MASS AND HEAT TRANSFER CHARACTERISTICS FOR LAMINAR FLOW IN A SHARP 180° TURN

خواص انتقال الحرارة والكتلة للسريان الرقائقى في مسار حاد ١٨٠°

M. Safwat Mohamed

Mechanical Power Engineering Department,
Faculty of Engineering, Mansoura University,
El-Mansoura 35516, Egypt
E-Mail: msafwat@mans.edu.eg

الخلاصة:

هذا البحث يقدم دراسة عددية لخواص انتقال الحرارة والكتلة للسريان الرقائقى في مسار حاد ١٨٠° وهى ذات علاقة بتبريد الدوائر الإلكترونية. وقد اعتبر السريان ثنائي الأبعاد نظرا لكبر geometrical aspect ratios المستخدمة في التطبيقات العملية لهذا السريان. وقد تم حل معادلات Navier–Stokes والطاقة باستخدام كود ذات قدرة عالية يستخدم نظرية الحجوم المحدودة. تمت الدراسة لسريان رقائقى حيث يتراوح رقم رينولدز (Re) بين ٥٠–١٠٠٠. أظهرت النتائج أن السريان يظل مستقرا حتى رقم رينولدز (Re) أقل من أو يساوى ٦٠٠. فى هذا النطاق يزداد طول منطقة إعادة الالتصاق تدريجيا مع زيادة رقم رينولدز (Re). أى زيادة بعد ذلك فى رقم رينولدز (Re) تؤدى لظهور السريان التذبذبى نظرا لتكون دوامات كبيرة الحجم ناشئة من الحافة الحادة. هذه الدوامات تنتشر فى حقل السريان وتسبب نقص شديد فى طول منطقة إعادة الالتصاق كما تسبب زيادة شديدة فى انتقال الحرارة بالحمل. وقد أظهرت دراسة العلاقة بين انتقال الحرارة وحقول السريان أنهما متلازمين بشدة.

ABSTRACT

Numerical studies of laminar flow and heat transfer around a sharp 180° turn, of especial relevance to electronic systems, are made. Two-dimensional unsteady simulations are considered because of the high geometrical aspect ratios ($AR > 5$) occurring in the practical application. A high-order time-accurate finite volume scheme was used to solve unsteady incompressible Navier–Stokes and energy equations. Simulations are performed for $50 \leq Re \leq 1000$. Predictions show that the sharp turn flow remains steady up to $Re \leq 600$. In this steady regime, the re-attachment length increases gradually with the Reynolds number. However, a further increase in the Reynolds number gives rise to oscillatory flow because of the large-scale vortices emanating from the sharp edge. These vortices dominate the flow field. Oscillations cause a considerable reduction in the re-attachment length and a significant increase in convective heat transfer. The correlation between the local heat transfer and the flow field is examined. Instantaneous friction coefficient C_f and Nusselt number Nu variations show that local heat transfer distributions correlate closely with the flow fields.

Keywords: Sharp 180° turn, Numerical simulation, Laminar; Oscillatory flow; Heat transfer.

INTRODUCTION

Numerous studies [1-7] have been performed to investigate flow and heat transfer characteristics in curved tubes in the absence of flow separation when the radius of curvature is relatively larger than the tube diameter. However, when a straight flow passage undertakes 180° bend, the combination of a secondary flow induced by the centrifugal force and a large-scale flow separation causes extremely complex flow and heat transfer phenomena at both the bend region and the subsequent straight-flow section. Neither mechanisms nor characteristics of flow and heat transfer in such passages have been fully explored.

The request of compact and high performance electronic system increases. So, their thermal control is becoming an ever-increasing subject. Careful thermal management is essential for the design of such systems. For electronic systems the Reynolds number (Re) range is typically $100 \leq Re \leq 1000$ [8]. Reynolds numbers can vary significantly in different regions of a single system. At Reynolds numbers relevant to electronics, flows can become unsteady. This can strongly affect

Accepted March 26, 2006

convective heat transfer. Also, the geometry is generally complex with many corners, recesses, and regions where flows are sharply turned. All of the above make the potential for the stimulation of an oscillatory flow relatively high (Tucker [8]). The electronic central processor unit (CPU) contains some of these attributes.

An extensive review of the application of computational fluid dynamics (CFD) to electronics is given by Tucker [9]. This shows that generally convective heat transfer due to unsteady separated flow around circuit boards has received relatively little attention compared to unsteady cooling over integrated circuit arrays. The exception to the above is the pioneering work of Ghaddar et al. [10] who performed laminar periodic grooved channel flow simulations. For Reynolds numbers less than a critical value Re_c the flow is found to be steady. Then, there is little transport of fluid between the main through flow and the groove area formed between the IC components. The flow undergoes a supercritical regular Hopf bifurcation at $Re = Re_c$. For $Re > Re_c$, cyclic flow oscillations which increase fluid transport to and from the groove are observed. They found that by using a sub-critical oscillation heat transfer could be increased by up to 15%. Similarly, Kim et al. [11] used an inflow oscillation to increase the heat transfer, finding a particular frequency for the maximum heat transfer enhancement. Unsteady flow, impinging jets have also been used to remove localized heat loads in electronics package [12-14].

Ghaddar et al. [15], and Patera and Mikic [16] used two-dimensional non-isothermal predictions to illustrate the potential for naturally enhancing heat transfer using the unsteadiness observed by Ghaddar et al. [10]. Amon and Mikic [17] and Amon [18] extend the above work, comparing heat transfer enhancement for flows where oscillations are induced passively by tripping, actively by flow modulation and naturally when $Re > Re_c$. Overall, when pumping losses are taken into consideration, passive heat transfer enhancement is found to be most effective. The above work uses a spectral element method [19-20]. The accuracy of this is initially demonstrated in Ghaddar et al.'s grooved channel work [10] by considering spatial development of a Tollmien–Schlichting (T–S) instability wave in plane channel flow. This flow is linearly stable up to $Re_c = 5772$ (Orszag, [21]) (based on the half-channel height and the center-line velocity). For $Re < Re_c$, instability shows a downstream decay. Importantly, all of the above grooved channel work assumes periodic flow.

Previous studies on the flow around sharp 180° turns have mostly focused on higher ($Re \geq 10^4$) Reynolds numbers [22-26]. At these Reynolds numbers, industrial applications include ventilation piping systems and inter-cooling passages in gas turbine blades. In contrast, for electronic systems the Reynolds number is much lower and typically in a range of $Re \leq 5000$.

The flow around a sharp 180° turn is considered as a simplification to the flow around circuit boards. Massive flow separation occurs as the flow passes around the bend and this at relatively low Reynolds numbers can cause an oscillatory downstream flow (Chung et al., [27]). In the work; of Ghaddar et al. [15], Kim et al. [11], and Chung et al. [14]; it is found that the flow oscillations can significantly affect laminar convective heat transfer. Therefore, understanding of the unsteady heat transfer in sharp 180° turns is essential.

The objective of the present investigation is to simulate the unsteady flow in a 180° sharp turn numerically. Flows at $50 \leq Re \leq 1000$ are employed using an efficient numerical approach. Due to the massive separation, the flow unsteadiness and heat transfer in these are much stronger than for U-turns. Unsteady flow characteristics and the related convective heat transfer are analyzed. Although the present work is heavily motivated by electronics, it also has strong relevance to other lower Reynolds number ventilation cases.

NOMENCLATURE

AR	aspect ratio.
C_f	friction coefficient
C_p	specific heat capacity.
d	plate thickness.
L	channel length.
g	gravitational acceleration.
h	channel height.

H	height of computational domain.
k	thermal conductivity of the fluid.
Nu	local Nusselt number.
P	pressure.
Pr	Prandtl number. $\mu C_P/k$
Re	Reynolds number, $U_m h/\nu$
t	time.
T	temperature.
U	bulk-mean velocity.
u, v	longitudinal and transverse mean velocity component.
x, y	Cartesian coordinates.
W	channel width.

Greek symbols

μ	dynamic viscosity of the fluid.
ν	kinematic viscosity of the fluid.
ρ	density of fluid.
$\Delta\tau$	dimensionless time step.

Subscripts

av	average.
i	inlet.
i	streamwise (x).
j	normal to the wall (y).
max	maximum.
min	minimum.
s	separation.
r	reattachment.
w	wall value.

PROBLEM FORMULATION

Figure 1 shows the flow configuration considered in this investigation. Flow enters the computational domain at the left end of the lower channel and exits at the left end of the upper one. The lower and upper channels are referred to as inlet and outlet channels, respectively. The length, height and width of the computational domain are L, H and W, respectively. The channel height is h and the plate thickness d. The Reynolds number is defined as $Re = U_m h/\nu$, where U_m is the bulk-mean velocity and ν is the kinematic viscosity.

In low Reynolds number laminar flow simulations, the two-dimensionality assumption has been commonly chosen when the aspect ratio (AR) is high. In the present investigation, $d/h = 0.1$ is chosen as representative of a typical electronics system value. In typical electronics systems, the aspect ratio (W/h, W/d) is generally high. Therefore, In the central part, the general flow structure can be regarded as two-dimensional. It is also worth noting that Brederode and Bradshaw [28] recommends $AR > 10$ to avoid significant side wall effects for a backward-facing step flow. In order to investigate the downstream flow recovery after the sharp bend, the computational domain has a long of, $L = 12h$.

GOVERNING EQUATIONS AND NUMERICAL METHOD

For two-dimensional unsteady laminar flows, continuity, Navier–Stokes and energy equations can be written in the following tensor form:

$$\frac{\partial u_i}{\partial x_i} = 0 \tag{1}$$

$$\frac{\partial u_i}{\partial t} + \frac{\partial}{\partial x_j}\left(u_i u_j\right) = -\frac{1}{\rho}\frac{\partial p}{\partial x_i} + \upsilon\frac{\partial^2 u_i}{\partial x_j^2} \tag{2}$$

$$\frac{\partial T}{\partial t} + \frac{\partial Tu_i}{\partial x_i} = -\frac{K}{\rho c_p}\frac{\partial^2 T}{\partial x_i^2} \tag{3}$$

In the above equations, u_i is the instantaneous velocity in the x_i direction, p is the pressure, and T is the temperature. Here ρ is the fluid density, K thermal conductivity and C_p the specific heat capacity. The subscripts i and j take values of 1 and 2 to denote the stream wise (x) and normal to the wall (y) directions, respectively.

Boundary conditions

No-slip velocity boundary condition ($u_i = 0.$) is applied on all walls. At the inlet, a parabolic velocity profile is provided. Temperature boundary conditions are set in order to approximate thermal conditions occurring in electronics. The temperature of the incoming flow is constant at T_i. The temperature of the lower wall, located at $y = h + d$ after bend is T_w. For relevance to heat transfer from circuit boards $T_w > T_i$ and the upper wall, located at $y = H$, is adiabatic. The temperature at the remaining walls is constant at T_i.

Numerical Scheme

All simulations have been carried out using *CAFFA* (Computer Aided Fluid Flow Analysis) code [29]. The numerical investigation is based on the solution of the complete Navier-Stokes and energy equations; Eqs. (2) and (3); using the Finite Volume Method on co-located body-fitted grids. Staggered grid arrangements are made, in which, velocity components are defined at the midpoints of cell sides to which they are normal while the pressure and temperature are defined at the center of the cell. The SIMPLE algorithm, Patankar [30], was applied to resolve the pressure-velocity coupling in conjunction with an Alternating Direction Implicit (ADI) scheme for performing the time evolution.

The computations of velocity and temperature fields are coupled. To start a computational cycle, guess fields of velocity, pressure and temperature are used. From these fields, corrected pressure and velocity fields are obtained by pressure and velocity iteration through continuity equation. From the initial temperature field and aforementioned corrected velocity field, a temperature distribution for the first cycle is calculated from the energy equation. This new temperature field and the foregoing corrected velocity and pressure fields are used to solve Navier-Stokes equations, Eqs. (2), to evaluate velocities for the next time increment. As such, in the subsequent cycles, solutions for velocities are obtained in two steps. First, the velocity components are advanced, using the previous state of flow to calculate accelerations caused by convections, viscous stresses, pressure gradients, and buoyancy interactions through a time step of duration $\delta\tau$. The explicit time increment may not necessarily lead to a velocity field with zero mass divergence in each cell. Second, pressure and velocity are adjusted by iterative process in order to ensure mass conservation in each cell. This iterative correction of explicitly advanced velocity fields through an implicit continuity equation is equivalent to solution of Poisson equation for pressure. The convective terms of Eqs. (2) are discretized by a weighted average of an upwind and central differencing scheme. After evaluating correct velocities, the energy equation is solved with successive over-relaxation technique to determine the temperature field. This solution scheme is continued until a periodic flow is obtained. The procedure avoids the need of pressure boundary conditions associated with the solution of Poisson equation or pressure.

The grid dependency was checked by using differenet grid sizes. Flows at low Reynolds number (steady state flow cases) are run on a 280 x 80 grid. Most simulations (unsteady state flow cases) are run on a 470 x 160 non-uniform grid. The effects of the temporal resolutions are investigated by successively halving time steps. Time steps of $\Delta t = 0.01$ are used at which no substantial differences are observed.

VALIDATION:

In this investigation, Laminar flow and heat transfer simulations for sharp bend flow are performed for $50 \le Re \le 1000$. To the best of the author's knowledge, there are no experimental data for this kind of flow. Consequently, the present numerical results cannot be compared directly with measurements. Instead, the validation of the numerical predictions has been performed with carefully selected test cases.

A widely used benchmark flow to examine the accuracy of numerical methods is the flow over a backward-facing step. This flow is an ideal test case for complex flow simulations because it involves flow separation, a free-shear layer, re-circulation, re-attachment, and redevelopment. The geometry is the same as in the experiments of Armaly et al. [31]. The expansion ratio of the step height (h) to the entrance channel height is 1:2 and the domain is $30h$. The calculated re-attachment length as a function of Re is compared with the experimental and numerical data of Armaly et al. [31] and the predictions of Kim and Moin [32], see Fig. 2. The present results compare well with the other data.

Another validation is the flow simulation in a three-dimensional, low-aspect ratio, U-bend. The flow configuration is chosen to match the experimental results of Hille et al. [33]. The duct has a curvature ratio $R/D = 6.5$, where R is the radius of curvature and D the hydraulic diameter. The inner width a and height b of the duct are taken as 1.0 (i.e., an aspect ratio of unity). The lengths of the duct before and after

the bend are taken as 10 times the hydraulic diameter. At inlet, a fully developed velocity profile is applied. The Reynolds number is defined as $Re = U_m D/\nu$. Simulations are performed for two Reynolds numbers, $Re = 200$ and 500. The corresponding Dean numbers ($K = Re\ (D/R)^{1/2}$) are $K = 78.45$ and 196.1, respectively. The radial variations of azimuthal velocity at various locations along the mid-span of the duct matches well with the experimental data of Hille et al. [32]. Fig. 3. shows the normalised azimuthal velocity versus the normalised radial location at duct mid-height and angle of turn, $\theta = 18°$, for ($Re = 500$). The results indicated that the code is able to simulate this kind of complex flow.

RESULTS AND DISCUSSION

Mean Flow Distributions

The numerical study indicated that, the flow is steady up to $Re \approx 600$. For $Re > 600$, the flow is found to be oscillatory du to the vortex shedding from the sharp corner. This can be observed from Fig. 4, showing the time history for the transverse velocity v at the measuting point ($x = 0$ and $y = 1.6$) for $Re = 500$, 700 and 1000. At $Re = 500$, velocity fluctuations decrease after an initial transient period ($0 \le t \le 45$), therefore, the flow field is quasi-steady. However, with increasing Reynolds number ($Re > 600$), oscillations are sustained and the flow becomes unsteady. Significant quasi-periodic velocity variations can be seen at $Re = 700$ and 1000. The dominant low frequency component corresponds to the vortex shedding from the sharp corner. Figure 5 shows more detailed frequencies in order to demonstrate the complexity of the flow field.

Time-mean streamlines and velocity vectors are shown in Figs. 6 and 7, respectively, for Reynolds numbers ($Re = 150$, 500, 700 and 1000). In the steady flow region ($Re \le 600$), the size of the re-circulation region increases with increasing Reynolds number. As the onset of the unsteadiness occurs ($Re > 600$), the size of the re-circulation region reduces significantly. It is obvious that flow unsteadiness significantly influences the mean flow field. The re-attachment length x_r is determined as a distance from the edge of the bend ($x = 11$) to a point where the time-mean velocity gradient (du/dy) at the outlet channel lower wall ($y = 1.1$) is zero. At $Re = 150$, the re-attachment length is $x_r = 3.34$. It increases to $x_r = 5.48$ at $Re = 500$. While it it reduces to $x_r = 2.10$ and 1.9 at $Re = 700$ and 1000 respectively. At $Re = 500$, the high velocity fluid near the upper wall is separated from the stagnant flow inside the re-circulation region. Consequently, there is negligible mixing between the two regions. Conversely, at $Re = 700$, the mixing inside the re-circulation zone is rather strong. Once the flow becomes oscillatory, the overall flow features become almost Reynolds number independent.

Friction coefficient and Nusselt number Distributions

To investigate the correlation between flow and temperature fields, the friction coefficient C_f and heat transfer Nu are analysed. The main focus is the outlet channel lower wall ($y = 1.1$).

The friction coefficient C_f and Nusselt number Nu are defined as:

$$C_f = (dU/dY)_w / Re \qquad (4)$$

Where U is the stream wise velocity normalised by U_m and Y is transverse distance normalised by h.

and
$$Nu = \frac{h}{\Delta T}\left(\frac{dT}{dy}\right)_w \qquad (5)$$

where ΔT is the temperature difference ($T_w - T_i$), T_w the wall temperature and T_i the inlet temperature.

Figure 8 shows the friction coefficient C_f distributions at the outlet channel lower wall ($y = 1.1$) for different values of Reynolds number. It can be seen that the reattachment length (x_{Cf} at $C_f \approx 0$) increases with the Reynolds number until $Re \approx 600$. Fig. 9. shows the minimum friction coefficient and its location as function of Re. The location of the negative peak (x_{Cf}) also moves downstream with the increasing Reynolds number. The minmum friction coeffient value becomes negative due to secondary vrotices as shown in Fig. 7. This peak value decreases, indicating stronger re-circulating motions. Then, a sudden change occurs for $Re > 600$. Also, the size of the re-circulation zone is reduced significantly . As the flow becomes oscillatory, friction coefficient C_f

distributions do not change much with increasing Re.

Figure 10 shows instantaneous streamlines at time intervals of Δt = 1.0 sec for flow at Re = 700. Large-scale vortices originating from the sharp corner are clearly seen. These move downstream at an almost constant velocity. The flow is quasi-periodic forming a complex unsteady flow cycle. It is clear that the large-scale vortex shedding dominates the whole flow field. The amplitude of the flow oscillations decays slowly until as it approaches the computational domain exit.

Figure 11 shows instantaneous velocity vectors at time intervals of Δt = 1.0 sec for flow at Re = 700. It demonstrates the significant changes caused by the flow oscillation. The flow inside the recirculation zone is active and the maximum reverse velocity is of the same order of magnitude as the main flow. This is consistent with the high friction coefficient C_f value at Re = 700 (Fig. 8).

Figure 12 shows the time-mean Nusselt number distribution along the channel exit lower wall, located at $y = h+d$ =1.1. As the flow moves downstream, Nusselt number Nu increases and attains a maximum. Then, due to the development of a boundary layer, it decreases steadily. The maximum Nusselt number, Nu_{max}, increases with Re. Also, for $Re \leq 600$, the Nu_{max} location moves downstream with increasing Re. Results show that the maximum Nusselt number occurs just downstream of the time mean re-attachment points. At Re = 500, Nu_{max} is an order of magnitude larger than Nusselt number Nu in the re-circulation zone. As the flow becomes oscillatory (Re = 700), the Nusselt number Nu distribution shows a very different pattern from the gradual steady regime ($Re \leq 600$) changes. Nusselt number Nu is increased significantly in the whole region. The Nu_{max} location suddenly moves upstream. Also, the region where Nusselt number Nu is small (Nu < 1) has almost disappeared. At further higher Reynolds numbers, the Nusselt number Nu distribution shows similar trends to that for Re = 700. These findings are consistent with the friction coefficient $C_f$distributions as shown in Fig. 8.

Figure 13 presentes the reattachment length x_r and Nusselt number Nu. In the figure, Nu_{12} represents Nusselt number Nu averaged along the wall ($1 \leq x \leq 12$). The reduction in x_r and increase in Nusselt number Nu with the onset of oscillatory flow (Re > 600) are obvious. To emphasise the effect of flow unsteadiness in the recirculation region, another Nu_5 average over a short distance ($1 \leq x \leq 5$) is provided. This region corresponds to the recirculation zone at Re = 300. Nu_5 increases significantly due to unsteadiness of the flow. The re-attachment length is also icluded in the figure to show the correlation between flow and temerature field.

Instantaneous friction coefficient and Nusselt number Distributions

Figure 14 shows instantaneous flow and temperature parameters for flow at Re = 700. Instantaneous temperature and flow parameters are analysed to understand the effect of unsteadness on the heat transfer characteristics. Fig. 14(a) and (b) demonstrates contour plots of instantaneous streamlines and temperature, respectively. The temperature field shows oscillatory behavior as a result of the downstream movement of large-scale vortices. Downwards motions between vortices enhance the heat transfer significantly. Chung et al. [14] observed similar characteristics in unsteady impinging jets.

Figure (14)c and d demonstrate instantaneous friction coefficient C_f and Nusselt number Nu distributions along the exit lower wall. The coparaison between Fig. (14)a and c indicated that, the location for minimum friction coefficient C_f is consistent with the location of the large-scale vortices. The coparaison between Fig. (14)c and d illustrated that, the secondary maximum Nusselt number occurs between the locations of flow separation (x_s) and reattachment (x_r). The local Nusselt number has a secondary maximum underneath the secondary vortex (Law and Masliyah [34]; Meola et al. [35]). A little upstream of x_s, the Nusselt number has a local minimum due to the thickening of the thermal boundary layer. In the main separation region, the correlation between heat transfer and flow field is not so good as further downstream. This is because, around the main separation region there are many smaller secondary vortices. Further downstream of the main separation region the small-scale vortices

merge to produce a more coherent flow field. Consequently, the correlation between heat transfer and flow field gets better.

CONCLUSION

Unsteady laminar flow around a sharp 180° turn is performed for $50 \le Re \le 1000$. Two-dimensional unsteady simulations are considered because of the high geometrical aspect ratios ($AR > 5$) occurring in the practical application. A high-order time-accurate finite volume scheme is used to solve unsteady incompressible Navier–Stokes and energy equations. The validation of code is checked against two benchmark flows. Verification results show good agreement with the available data.

The following conclusions may be drawn from the present investigation:

1- The flow in the sharp bend remains steady until $Re < 600$. However, a further increase in the Reynolds number increases the oscillatory flow.

2- The analysis shows that the unsteadiness of the flow field is mainly caused by the dominant low frequency component corresponds to the vortex shedding from the sharp corner.

3- A significant reduction in the re-attachment length and a considerable increase in convective heat transfer is caused by oscillations. For $Re = 700$ (oscillatory flow), the re-attachment length is reduced to less than half and the Nusselt number increases several times compared to $Re = 600$ case.

4- The onset of flow oscillations is important since it significantly enhances heat transfer.

5- The correlation between flow structure and heat transfer is found to be strong.

REFERENCES

[1] Cheng K.C., Akiyama M., 1970, 'Laminar forced convection heat transfer in curved rectangular channels', International Journal of Heat and Mass Transfer 13, pp 471-490.

[2] Metzger D.E., Plevich C.W., Fan C.S., 1984, 'Pressure loss through sharp 180 deg turns in smooth rectangular channels', Trans. ASME, Journal of Engineering for Gas Turbines and Power 106, pp 677-681.

[3] Humphrey J.A.C., Iacovides H., Launder B.E., 1985, "Some numerical experiments on developing laminar flow in circular sectioned bends", J. Fluid Mech., 154, pp 357-375.

[4] Kajishima T., Miyake Y., Inaba T., 1985, "Numerical simulation of laminar flow in curved ducts of a rectangular cross section, Trans. JSME, B 45 :(503), pp 1594-1601.

[5] Sugiyama S., Yamamoto M., Hayashi T., 1987, "Flows in a curved rectangular channel (2nd report, velocity measurements in the developing region of laminar flow by using LDV)", Trans. JSME,. B 53(487), pp 750-756.

[6] Cheng K.C., Yuen F.P., 1987, "Flow visualization studies on secondary flow patterns in straight tubes downstream of a 180 degree bend and in isothermally heated horizontal tubes", Trans. ASME, Journal of Heat Transfer, pp 49-54.

[7] Hwang G.J., Chao C.H., 1991, "Forced laminar convection in a curved isothermal square duct", Trans. ASME Journal of Heat Transfer 113, pp 48-55.

[8] Tucker, P.G., 2001, "Computation of unsteady internal flows", Kluwer Academic Publishers.

[9] Tucker, P.G., 1997, "CFD applied to electronic systems: a review", Trans. IEEE (CPMTA) 20 (4), pp 518–529.

[10] Ghaddar, N.K., Karczak, K.Z., Mikic, B.B., Patera, A.T., 1986, "Numerical investigation of incompressible flow in grooved channels, Part1. Stability and self-sustained oscillations", J. Fluid Mech. 163, pp 99–127.

[11] Kim, S.Y., Kang, B.H., Hyun, J.M., 1997, "Forced convection heat transfer from two heated blocks in pulsating channel flow", Int. J. Heat Mass Transfer 41, pp 625–634.

[12] Beitelmal, A.H., Saad, M.A., Patel, C.D., 2000, "The effect of inclination on the heat transfer between a flat surface and an impinging two-dimensional air jet", Int. J. Heat Fluid Flow 21, pp 156–163.

[13] Chung, Y.M., Luo, K.H., Sandham, N.D., Williams, J.J.R., 2001, "Direct numerical simulation of an impinging jet", In: Lindborg, E., Johansson, A., Eaton, J., Humphrey, J., Kasagi, N., Leschziner, M., Sommerfeld, M. (Eds.), Turbulence and

Shear Flow Phenomena, vol. 2. Universities service US AB, Stockholm, pp. 271–276.

[14] Chung, Y.M., Luo, K.H., Sandham, N.D., 2002, "Numerical study of momentum and heat transfer in unsteady impinging jets", Int. J. Heat Fluid Flow 23, pp 592–600.

[15] Ghaddar, N.K., Magen, M., Mikic, B.B., Patera, A.T., 1986, "Numerical investigation of incompressible flow in grooved channels, Part 2. Resonance and oscillatory heat-transfer enhancement", J. Fluid Mech. 168, pp541–567.

[16] Patera, A.T., Mikic, B.B., 1986, "Exploiting hydrodynamic instabilities. Resonant heat transfer enhancement", Int. J. Heat Mass Transfer 29(8), pp 1127–1138.

[17] Amon, C.H., Mikic, B.B., 1990, "Numerical prediction of convective heat transfer in self-sustained oscillatory flows", J. Thermophys. 4(2), 239–246.

[18] Amon, C.H., 1992, "Heat transfer enhancement by flow destabilization in electronic chip configurations", J. Electron. Packaging pp 114, 35–40.

[19] Patera, A.T., 1984, "A spectral element method for fluid dynamics: laminar flow in a channel expansion" J. Comput. Phys. 54, pp 468–488.

[20] Amon, C.H., 1993, "Spectral element-Fourier method for transitional flows in complex geometries", AIAA J. 31 (1), pp 42–48.

[21] Orszag, S.A., 1971, "Accurate solution of the Orr–Sommerfeld stability equation", J. Fluid Mech. 50, pp 689–703.

[22] Metzger, D.E., Sahm, M.K., 1986, "Heat transfer around sharp 180° turns in smooth rectangular channels", ASME: J. Heat Transfer 108, pp 500–506.

[23] Chyu, M.K., 1991, "Regional heat transfer in two-pass and three pass passages with 180° sharp turn", ASME: J. Heat Transfer 113, pp 63–70.

[24] Hirota, M., Fujita, H., Syuhada, A., Araki, S., Yoshida, T., Tanaka, T., 1999, "Heat/mass transfer characteristics in two-pass smooth channels with sharp 180° turn", Int. J. Heat Mass Transfer 42, pp 3757– 3770.

[25] Mochizuki, S., Murata, A., Shibata, R., Yang, W.-J., 1999, "Detailed measurements of local heat transfer coefficients in turbulent flow through smooth and rib-roughened serpentine passages with a 180° sharp bend", Int. J. Heat Mass Transfer 42, pp 1925–1934.

[26] Liou, T.-M., Chen, C.-C., Tzeng, Y.-Y., Tsai, T.-W., 2000, "Non-intrusive measurements of near-wall fluid flow and surface heat transfer in a serpentine passage", Int. J. Heat Mass Transfer 43, pp 3233–3244.

[27] Chung, Y.M., Tucker, P.G., Luo, K.H., 2001, "Large-eddy simulation of complex internal flows" In: Geurts, B.J., Friedrich, R., Metais, O. (Eds.), Direct and Large-Eddy Simulation, vol. IV. Kluwer Academic Publishers, The Netherlands, pp. 373–380.

[28] Brederode, P., Bradshaw, P., 1978, "Influence of the side walls on the turbulent center-plane boundary-layer in a squareduct", ASME: J. Fluids Engng. 100, pp 91–96.

[29] Ferziger, J.H., and Perić, M., 1996, "Computational Methods for Fluid Dynamics", *Springer-Verlag*, Berlin Heidelberg

[30] Patankar, S.V., 1980. "Numerical Heat Transfer and Fluid Flow", McGraw-Hill, New York.

[31] Armaly, B.F., Durst, F., Peieira, J.C.F., 1983, "Experimental and theoretical investigation of backward-facing step flow", J. Fluid Mech. 127, pp 473–496.

[32] Kim, J., Moin, P., 1985, "Application of a fractional-step method to incompressible Navier–Stokes equations" J. Comput. Phys. 59, pp 308–323.

[33] Hille, P., Vehrenkamp, R., Schulz-Dubois, E.O., 1985, "The development and structure of primary and secondary flow in a curved square duct" J. Fluid Mech. 151, pp 219–241.

[34] Law, H.-S., Masliyah, J.H., 1984, "Mass transfer due to a confined laminar impinging two-dimensional jet", Int. J. Heat Mass Trans. 27 (4), pp 529–539.

[35] Meola, C., Luca, L., Carlomagno, G.M., 1996. Influence of shear layer dynamics on impingement heat transfer", Exp. Therm. Fluid Sci. 13, pp 29–37.

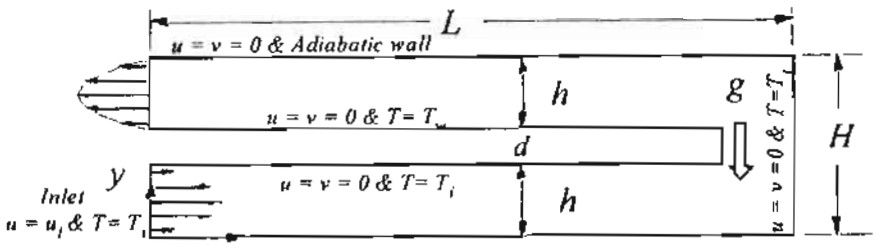

Fig. 1. Computational domain and boundary conditions.

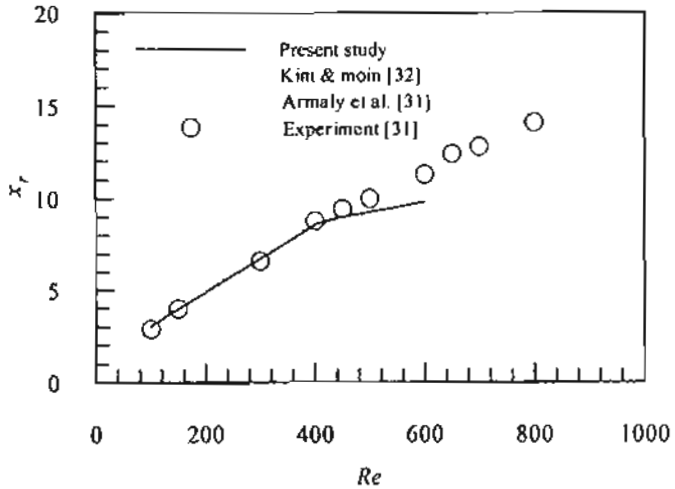

Fig. 2. Variation of the re-attachment length x_r with Reynolds number for the flow over a backward-facing step.

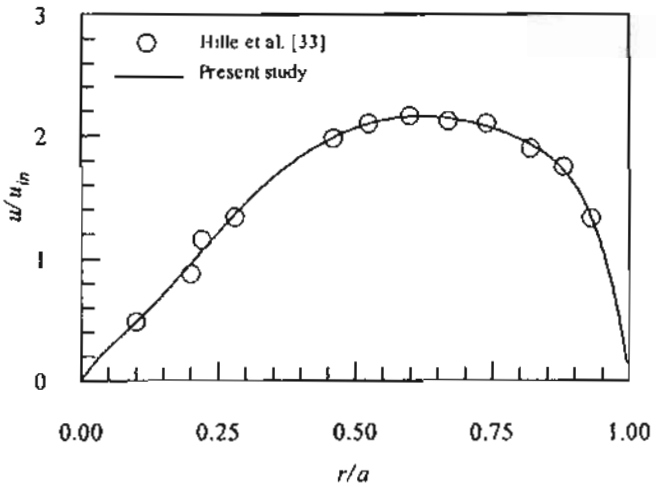

Fig. 3. Normalised azimuthal velocity versus the normalised radial location at duct mid-height and $\theta = 18^{\circ}$ (Re = 500)

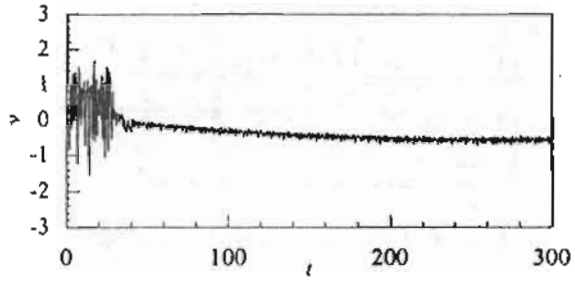

a) Re =500

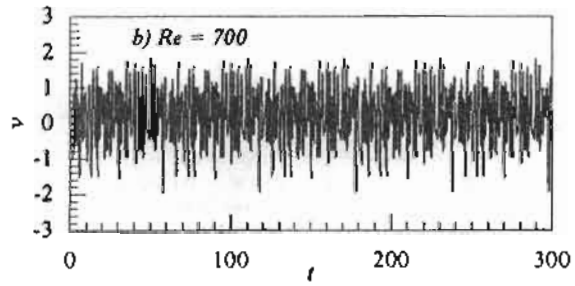

b) Re = 700

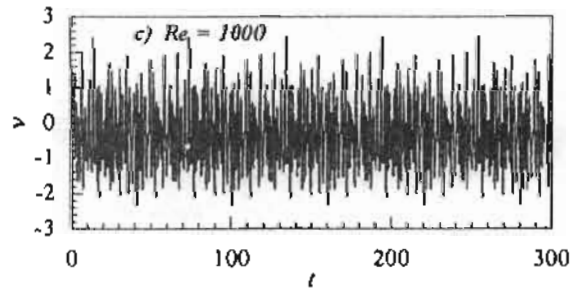

c) Re = 1000

Fig. 4. Instantaneous transverse velocity *v* at the point ($x = 0$, $y = 1.6$) for *Re* = 500, 700, 1000.

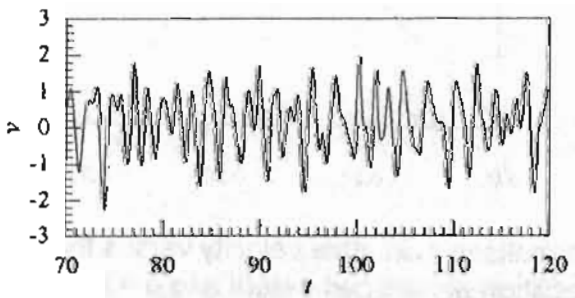

Fig. 5. Instntaneous transverse velocity *v* for *Re* = 700 at point ($x = 12$, $y = 1.6$)

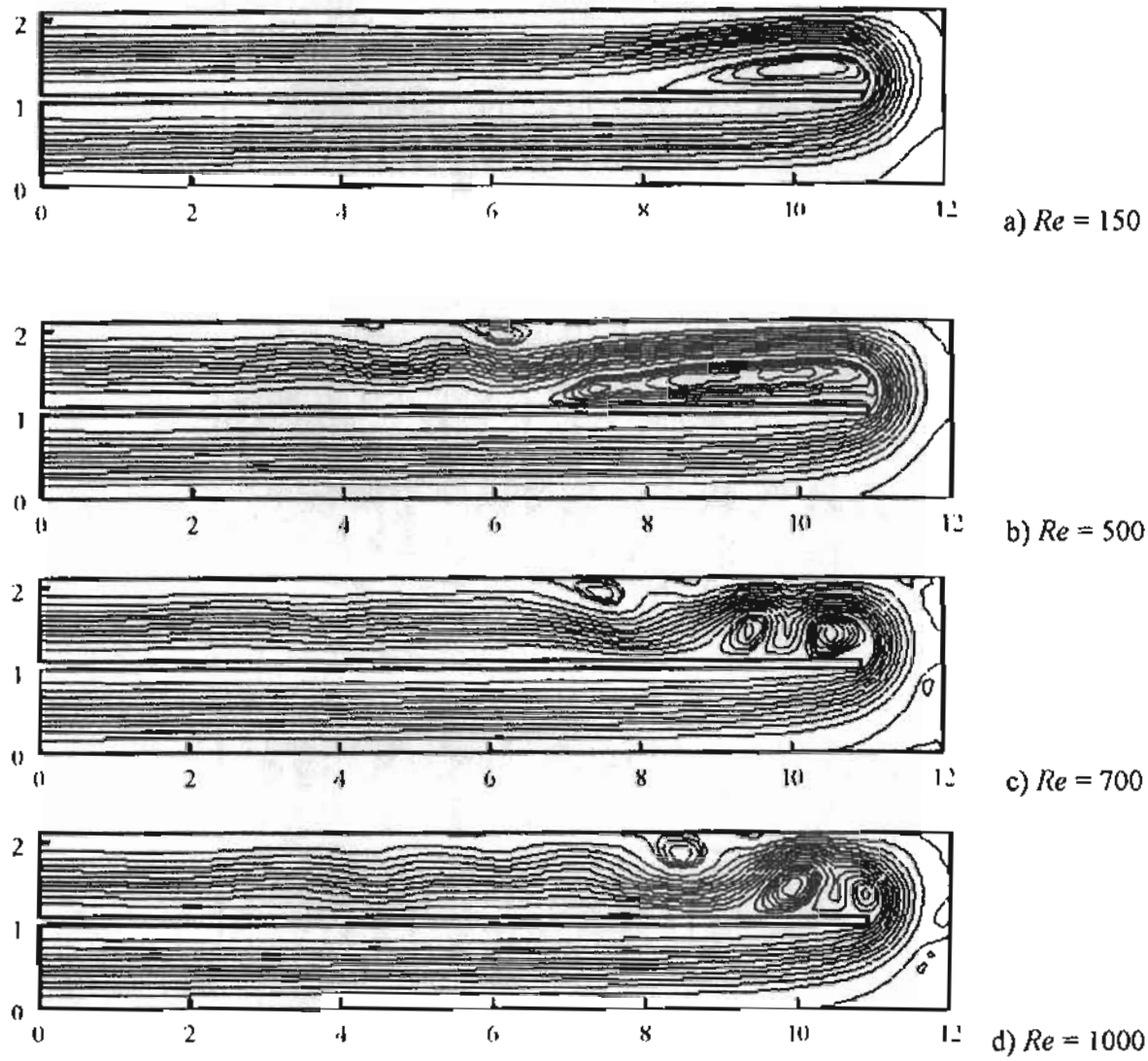

Fig. 6. Contours of time-mean streamlines at different Reynolds numbers.

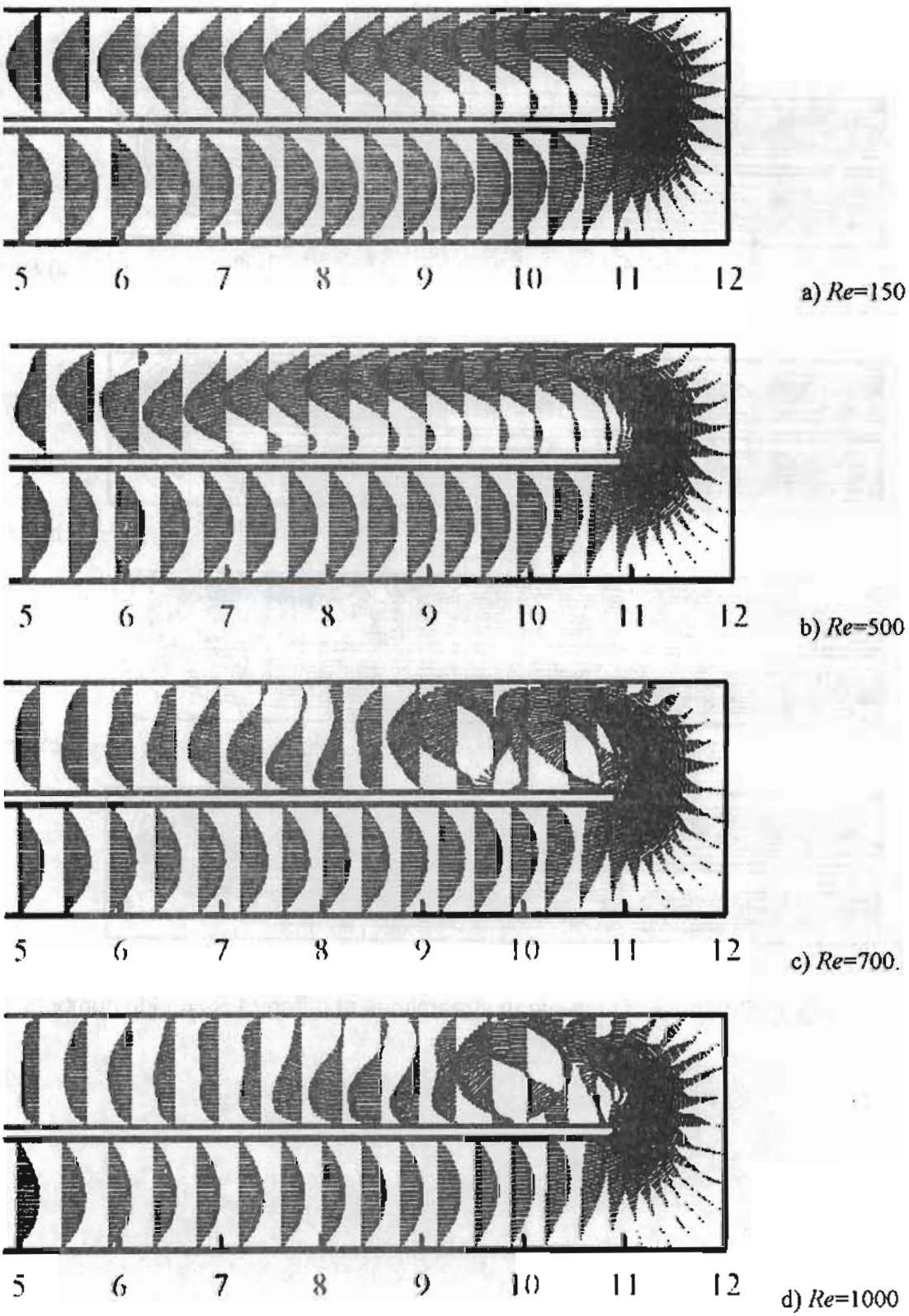

Fig. 7. Velocity vector plots for time-mean flow field at different Reynolds numbers.

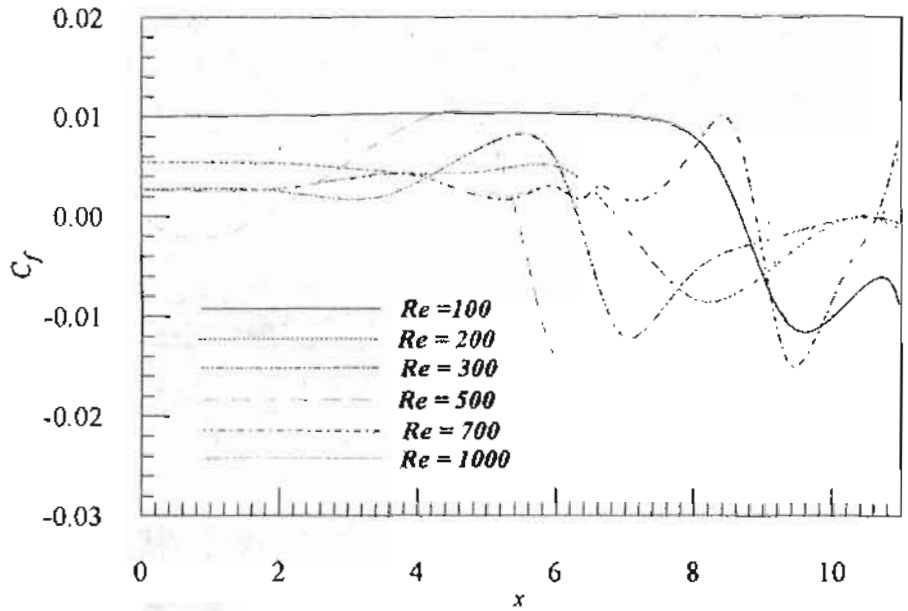

Fig. 8. Friction coefficient distribution along the lower wall (y = 1.1) at different *Re*.

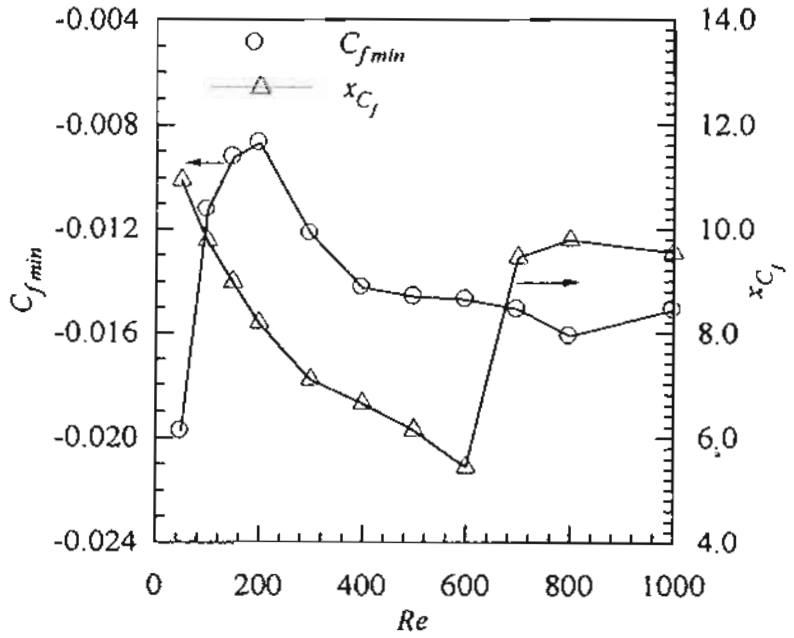

Fig. 9. The minimum friction coefficient and its location as a function of *Re*

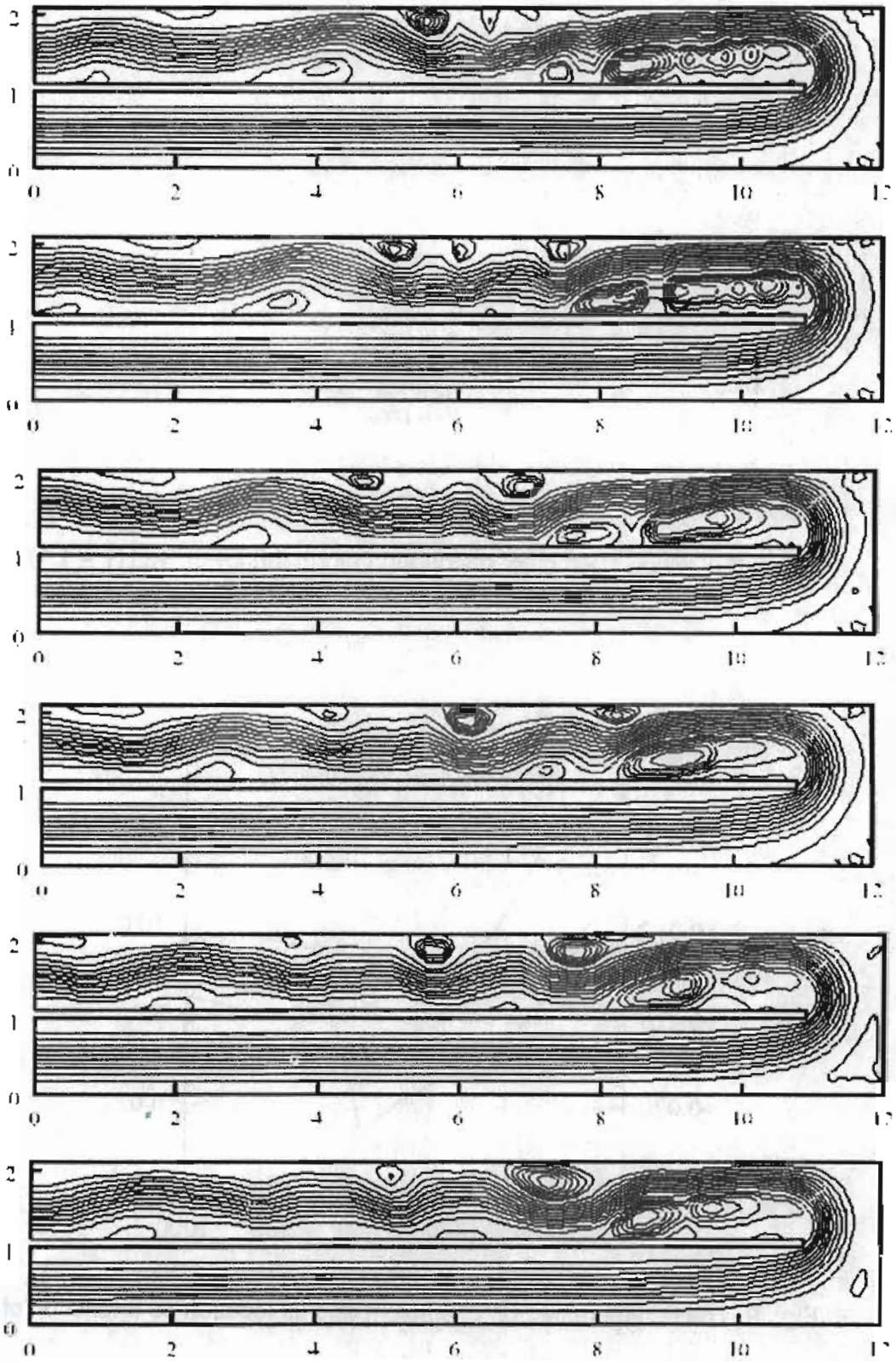

Fig. 10 Contours of streamlines at Re = 700 for time intervals Δt =1.0 sec

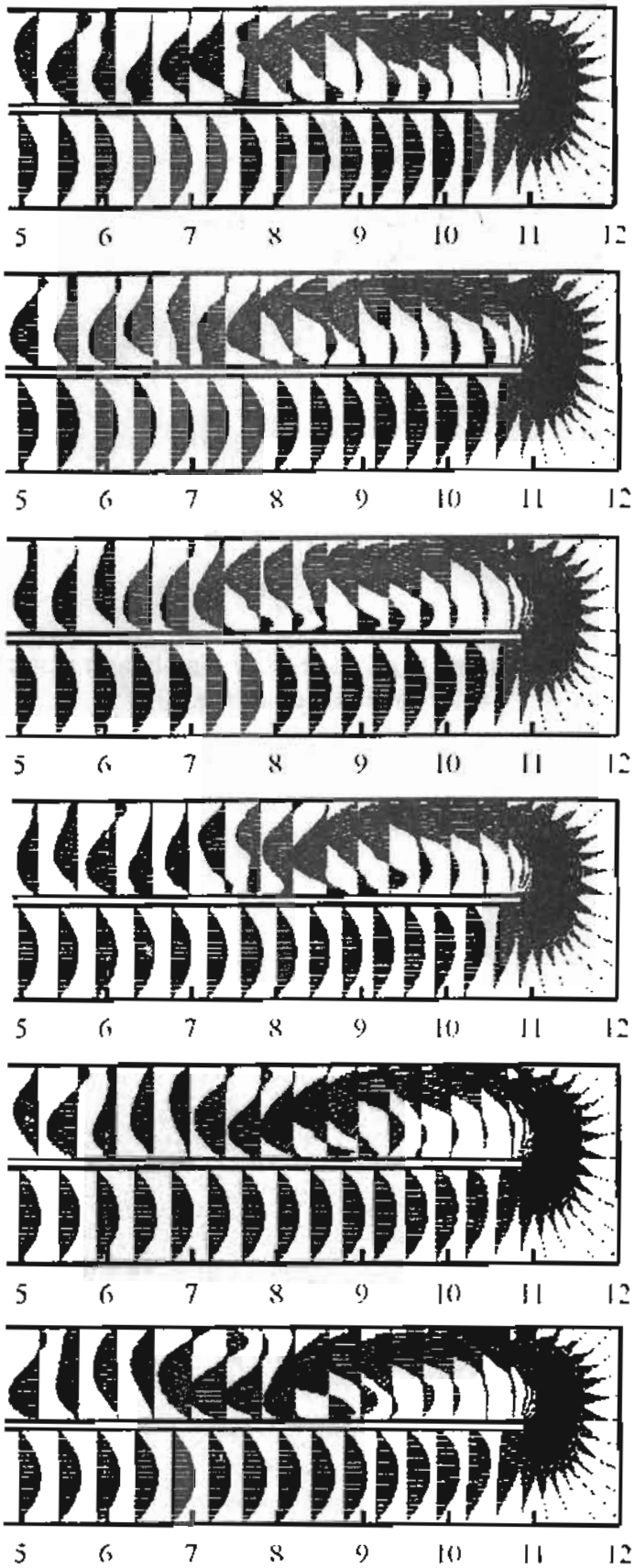

Fig. 11 Velocity vector plots of instantaneous flow field at Re = 700 for time intervals Δt =1.0 sec.

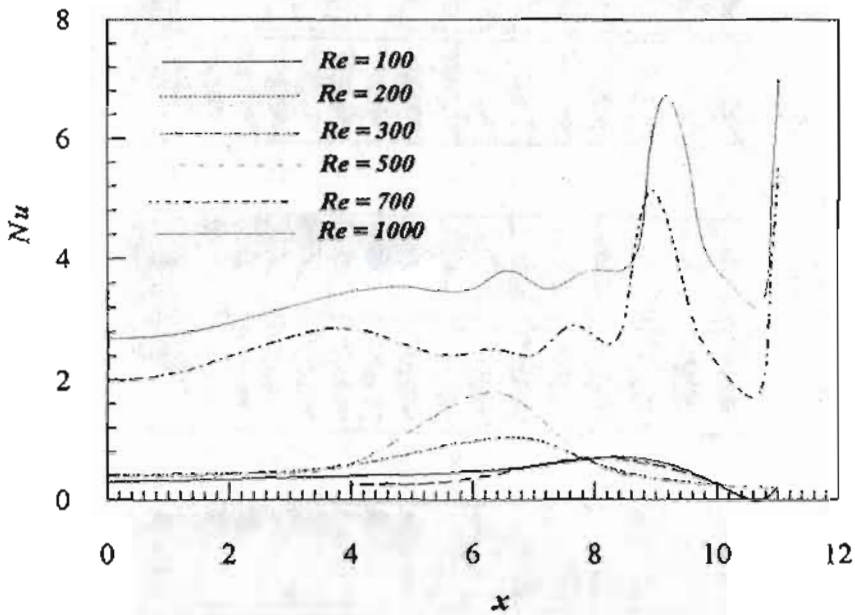

Fig. 12. Time-mean Nusselt number distribution along the exit lower wall (y = 1.1) as function of *Re*.

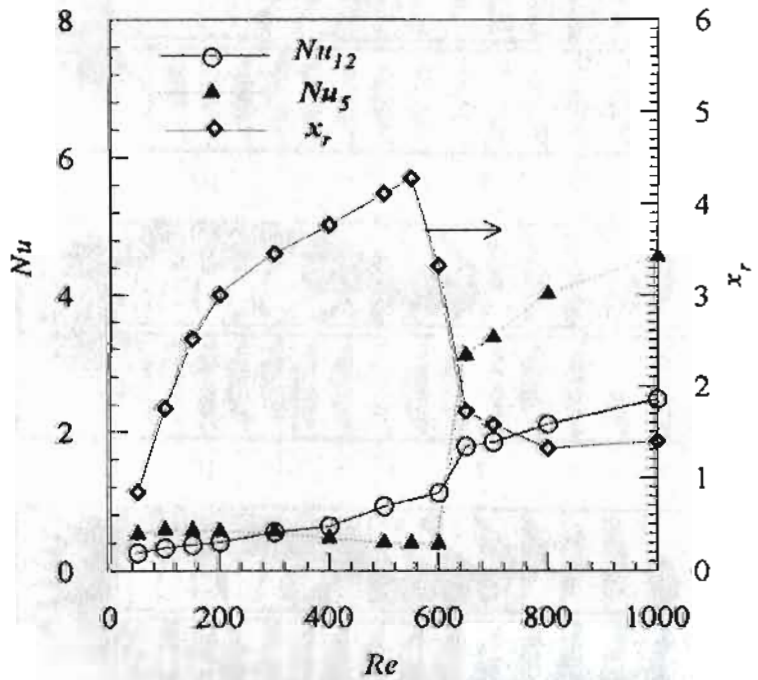

Fig. 13. Re-atachement length x_r and Nu_{av} as function of *Re*

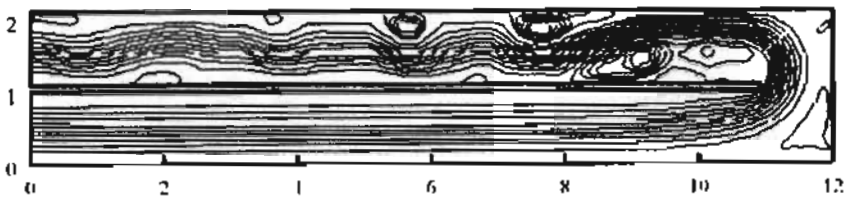

a) Instantaneous streamlines

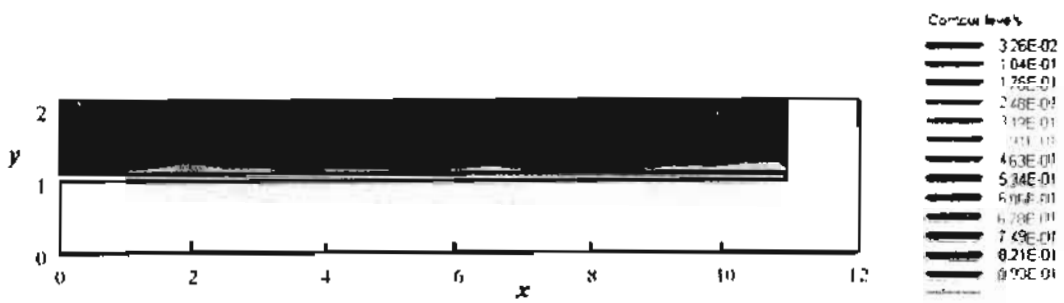

b) Instantaneous isotherms

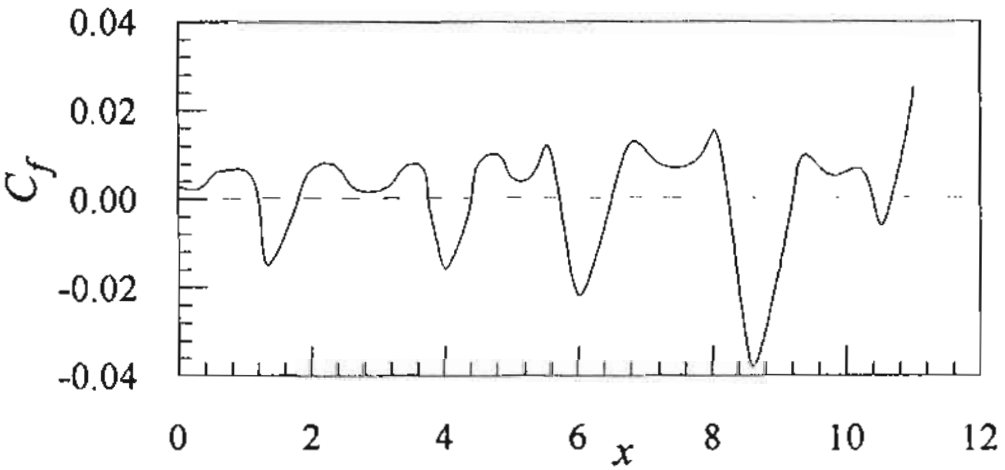

c) Instantaneous friction coefficient distributions.

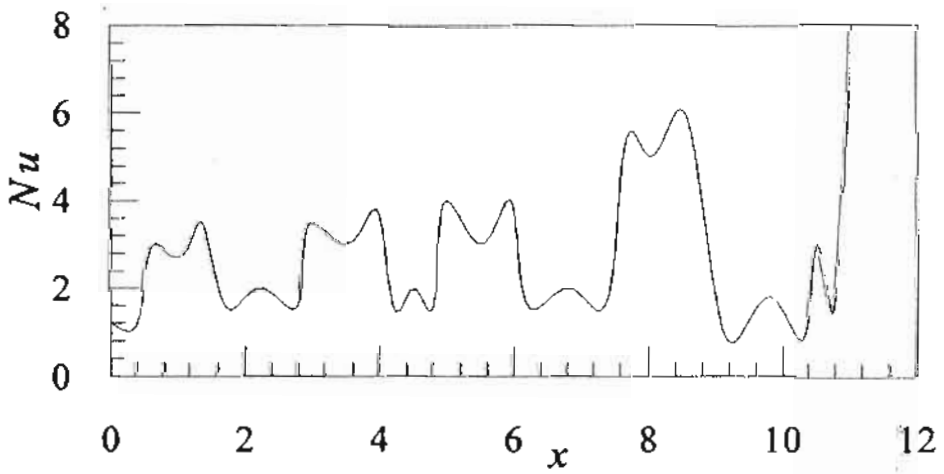

d) Instantaneous Nussult number distributions.

Fig. 14. Instantaneous flow and temperature parameters.